Reducibility of Cu-zeolites and stability of Cu$^+$ monocarbonyl adducts: Qualitative and quantitative relationships from MCR-XAS and DFT

Gabriele Deplano [a], Matteo Signorile [a,*], Cesare Atzori [b], Davide Salusso [b], Elisa Borfecchia [a], Valentina Crocellà [a], Silvia Bordiga [a]

[a] *Department of Chemistry, NIS and INSTM Reference Centre, Università di Torino, Via P. Giuria 7, 10125 and Via G. Quarello 15/A, 10135 Torino, TO, Italy*
[b] *European Synchrotron Radiation Facility, 71 Avenue des Martyrs, CS 40220, 38043 Cedex 9 Grenoble, France*

ARTICLE INFO

ABSTRACT

A series of Cu-exchanged zeolites differing in framework topology and composition are studied through in situ X-ray Absorption Spectroscopy (XAS) to highlight differences in reducibility depending on the characteristics of the different samples. After reduction at high temperature in NH$_3$, the samples are exposed to CO at 50 °C followed by a temperature-programmed desorption to study the different stability of carbonyl species forming on the Cu$^+$ sites. Multivariate Curve Analysis applied to the XAS data allows extracting concentration profiles and pure spectral profiles on the species involved during several steps of the reaction. While all the samples are quantitatively reduced after treatment in NH$_3$, the stability of the [Cu(CO)]$^+$ sites shows a dependence on the topology of the materials. DFT calculations on possible sites occupied by Cu in the different frameworks are consistent with the stability trends observed experimentally and, together with isothermal volumetric CO adsorption data, confirm the particular instability of the Cu$^+$-monocarbonyls formed in the CHA framework.

1. Introduction

Cu-exchanged zeolites are widely studied materials for their performance on several relevant reactions, such as the direct conversion of methane to methanol (DMTM) [1] and the NH$_3$-mediated selective catalytic reduction (SCR) of NO$_X$ in Diesel engine exhaust [2]. The reactivity of such materials as catalysts is usually based on the Cu^{2+}/Cu$^+$ redox cycle [3] as a means to promote redox reactions on the respective substrate. To better understand (and possibly enhance) the performance of these materials, in-depth investigation of their properties in conditions as close as possible to the ones involved in the reaction is of paramount importance. For this task, several techniques have been developed and applied, comprising in situ and *operando* spectroscopies [4–9], computational modelling [10–15], diffraction [1,16,17], electron microscopy [18] and more [19,20]. Due to the importance of the Cu redox cycle in the catalytic activity, the quantification of the relative amount of Cu^{2+}/Cu$^+$ species at any moment of the reaction is a key information for mechanistic elucidation. While Cu^{2+} can be detected by several experimental techniques, Cu$^+$ can be more challenging to quantitatively assess: for instance, the d [10] electronic configuration of such species excludes the use of EPR spectroscopy, and the absence of

d-d transition bands in UV-Vis spectroscopy also hinders the characterization. Even when Cu$^+$ sites are not directly involved in the reactions under study (for instance, in DMTM the proposed active species most often involve Cu^{2+} adducts), the reducibility of the Cu (and thus the reversibility of the redox cycle) has been correlated with catalytic performance [21]. X-ray Absorption Spectroscopy (XAS) is widely used as the main spectroscopic technique for quantitative assessment in this field, due to its sensitivity, element-selectivity and the possibility to perform in situ and *operando* experiments with relative ease. Data treatment procedures such as Linear Combination Fit (LCF) can then be used to extract the relative amounts of Cu components in different oxidation states and coordination environment based on previously acquired spectra of standard materials. While quantification through LCF is often challenging for solid materials, due to the lack of representative and/or easily reproduceable standards, statistical approach such as Multivariate Curve Resolution (MCR) have been successfully applied to several cases [22–24], showing good performance also for difficult cases. One of the main drawbacks of this technique is, however, the fact that it is still mostly accessible through large scale facilities (i.e., synchrotron sources). Recently, some attempts have been made to find an alternative approach to obtain the same information; a recent

publication from our group provided a simple way to titrate Cu^+ in Cu-ZSM-5 materials by means of broadly available lab instrumentation (such as isothermal volumetric adsorption and/or infrared spectroscopy), exploiting CO as a probe molecule at room temperature and low partial pressure [25]. It has been widely proved that under such conditions, CO selectively and irreversibly binds Cu^+ to form stable monocarbonyl adducts [26–29], that can then be used to titrate the amount of Cu^+ in the materials.

In this work, we investigate the reduction behaviour of a series of Cu-exchanged zeolites by high temperature (500 °C) reduction in the presence of NH_3 via MCR-assisted XAS. The pre-reduced materials are then cooled down to 50 °C and exposed to CO as a probe molecule, to directly assess the reversibility of the interaction of CO with these materials. A TPD protocol is subsequently applied on the materials to check the stability range of these adducts and how the decomposition takes place. Six Cu-zeolites of different topologies that are relevant for catalytic applications (e.g., CHA, MOR and MFI) and with different compositions in terms of Al and Cu content are explored in order to highlight framework- and composition-specific trends. The data are then compared with volumetric results and DFT calculations to validate and rationalize these specific differences.

2. Experimental

2.1. Materials

All the materials mentioned in this paper have been synthesised and characterized in previous studies. Details about the synthetic procedures, composition and characterization methodologies can be found in the respective references listed in Table 1, in which the Si/Al and Cu/Al ratios are also reported for all samples.

2.2. Methods

2.2.1. X-ray absorption spectroscopy

The in situ XAS data were collected at the BM23 beamline [33] of the European Synchrotron Radiation Facility (ESRF), under the beamtime awarded through the CH-6264 proposal [34]. The Microtomo [35] reactor cell, developed by the ESRF sample environment group, was chosen as sample environment. The powdered Cu-zeolites were prepared in the form of self-supporting pellets of 1.3 cm diameter with masses optimized for transmission-mode XAS measurements (ca. 40 mg, resulting in $\Delta\mu x=$ in the range 0.6–1.0 with total absorption after the edge of less than $\mu x=2.5$ for all samples) and placed inside the reactor cell. The temperature of the sample was controlled by the heating system integrated in the Microtomo cell. The total gas flow rate and the composition of the feed were adjusted by a set of mass flow controllers controlled by a remote terminal. The in situ Cu K-edge spectra were acquired in transmission mode, employing a double-crystal Si(111) monochromator to scan the incident energy, and ionization chambers to detect incident (I_0) and transmitted photons (I_1). A Cu metal foil was measured simultaneously with all the collected XAS spectra by means of a third ionization chamber (I_2), for energy calibration purposes. [36,37] The chambers were filled with a He/Ar mixture up to 2 bar with Ar partial pressure of 0.1 and 0.3 bar for I_0 and $I_{1,2}$ chambers, respectively.

Table 1
List of Cu-zeolites used in this work. All Si/Al and Cu/Al are reported as molar ratios.

Name	Si/Al	Cu/Al	Reference
(0.48)Cu-CHA(15)	15	0.48	[30]
(0.35)Cu-CHA(5)	5	0.35	[30]
(0.32)Cu-MOR(11)	11	0.36	[31]
(0.21)Cu-MOR(6.5)	6.5	0.21	[32]
(0.48)Cu-MFI(25)	25	0.48	[25]
(0.35)Cu-MFI(11.5)	11.5	0.35	[25]

The XAS signal was monitored as a function of time/temperature during the treatment steps, with acquisitions of ca. 2 min/scan in the 8830–9800 eV energy range. Spectra were collected in continuous mode with energy step of 0.3 eV, then were rebinned with constant energy steps of 5 eV in the pre-edge region (8928 – 8960 eV) and 0.3 eV in the XANES region (8960 – 9050 eV); a uniform sampling step in k-space of 0.08 $Å^{-1}$ was adopted in the extended region of the spectra. The energy ranges in the XANES scans analysed in this work were aligned using the simultaneously measured data for the Cu metal foil and normalized to unity edge jump. A custom Python-based script based on the Larch library [38] was employed for data alignment and normalization.

2.2.2. XANES statistical analysis and multivariate curve resolution

All the analysed XANES datasets comprised a range of spectra in the range 8070–9020 eV, with the number of spectra depending on the considered treatment step (vide infra). The XANES spectra collected throughout this work were analysed sample-wise via a Multivariate Curve Resolution (MCR) approach. [22,39,40] This technique involves the decomposition of experimental data in a set of pure spectra and concentration profiles, which can be used as qualitative and quantitative descriptive tools when a mixture of several species is present. An initial guess was generated via a Principal Component Analysis (PCA) of the experimental data, which provides a set of pure spectra based on the selected number of Principal Components (PC); the PCs are then used to initialize the Alternating Least Squares (ALS) algorithm, an iterative process that provides the spectra and concentration profiles upon convergence. The number of relevant PCs (n) for each instance was selected by locating the elbow point of the relative Scree plot (corresponding to the kth PC), visually inspecting the residual variances and evaluating the goodness of fit in the interval k-$1 \leq n \leq k + 1$. The convergence tolerance on the Lack of Fit (LOF) parameter for two successive iterations was set to 0.1%. After selection of the PCs, the MCR-ALS routine was initialized using the SIMPLISMA method [40]. XANES spectra are particularly suited for MCR-ALS analysis, since the element-selective characteristic of this technique allows to exploit some constraint that greatly enhance the efficiency of the algorithm, i.e., non-negativity of both spectral and concentration profiles, as well as closure for concentration profiles (i.e., summing to 1) can be employed to drive the algorithm toward a stable solution. [41] Indeed, in all cases convergence was achieved in less than 25 iterations, with final LOF values < 0.5%. Quality of reproduction of the experimental data was evaluated through the $\%R_{Factor}$, defined as:

$$\%R_{Factor} = \frac{\sum_{i,j}|\boldsymbol{D} - \boldsymbol{D}^{PCA}|}{\sum_{i,j}|\boldsymbol{D}|}$$

where $\boldsymbol{D}$ and $\boldsymbol{D}^{PCA}$ are the original and the PCA reconstructed dataset, while the subscripts i and j are the respective rows and columns. For every dataset, the $\%R_{Factor}$ was > 99.999%.

2.2.3. Isothermal volumetric adsorption measurements

Carbon monoxide (supplied by Sapio SRL, 99.99998% purity grade) adsorption isotherms were measured on a commercial volumetric apparatus (Micromeritics ASAP 2020) at 50 °C.

The samples were mortar ground and pelletized, in order to prevent any powder residues from moving out of the cell, while exposing to gas/vacuum treatment. The pellets were then inserted in a custom adsorption cell (Fig. S1) [42]. The sample temperature was kept constant by using an external isothermal liquid bath (Julabo F25-EH). Prior to the measurements, Cu-zeolite pellets were treated at high temperature on a vacuum line equipped with a turbomolecular pump; full details on the treatment can be found in the next section. After treatment, a primary CO adsorption measurement was performed on the sample, followed by an outgassing time interval of 2 h and a secondary CO adsorption run. As described in a previous publication [25], the difference between the primary and the secondary adsorption isotherms yields the amount of

irreversibly bound CO per gram of material, which can then be converted (supposing a 1:1 ratio between Cu^+ and CO) to the amount of Cu^+ through the equation:

$$Cu^+(\%) = CO \quad uptake \quad \left(\frac{mmol_{CO}}{g}\right) * formula \quad weight \quad \left(\frac{g}{mmol_{Cu}}\right) * 100$$

2.3. Treatment protocols

For the in situ XAS measurements, the same treatment procedure was applied to all samples, as shown in Fig. S2 and briefly described in the following. The gas employed for the experiments were supplied to the ESRF and consisted of the following: NH_3, 0.4 mol% in He (Air Products); CO, 5 mol% in He (Air Liquide); O_2, pure (Air Liquide); He, pure (Air Products). The sample was heated in a pure O_2 flow from room temperature to 500 °C with a ramp of 5 °C/min and kept at the same temperature for 10 min. After a He flush for 15 min, the sample was exposed to NH_3 (0.4 mol% mixture in He) at the same temperature for 40 min. He was dosed again to the sample for 80 min at 500 °C; the inert environment was kept while ramping down to 50 °C, after which the sample was kept in isothermal conditions for 10 more minutes. The sample was then exposed to CO (5 mol% mixture in He) for 15 min, and subsequently flushed with He for 120 min. Finally, the temperature was raised from 50 °C to 500 °C in He with a ramp of 5 °C/min. Mass flow controllers were calibrated for each mixture and used to keep a constant gas flow of 30 ml/min for each step of the procedure.

For all volumetric experiments, the following activation protocol was employed. The sample cell was heated from room temperature to 500 °C with a ramp of 5 °C/min under dynamic vacuum (residual pressure $< 10^{-3}$ mbar). O_2 (100 mbar) was then dosed and kept in contact with the sample at the same temperature for 30 min. The sample was then outgassed at the same temperature for 40 min. In this way, we brought all the samples to their most oxidized state. Then, a controlled NH_3 treatment was performed in order to maximize the amount of Cu^+ species. Previous studies on the topic showed that high temperature treatment in the presence of NH_3 leads to a Cu^+ content in the 75–92% range; [25,32] this is further confirmed in the present study (vide infra). Accordingly, 100 mbar of NH_3 were dosed on the sample at 500 °C for 30 min. Finally, outgassing was performed at the same temperature until a residual pressure of $< 10^{-3}$ mbar was achieved, then the sample was cooled down to room temperature. This procedure aims at maximizing the amount of highly uncoordinated Cu^+ that can be probed by CO.

2.4. Computational details

The adsorption of CO on the different Cu-zeolites studied experimentally was simulated at DFT level of theory by means of the CRYSTAL17 periodic code [43]. For each framework, Cu^+ substitution was studied at different positions, aiming at accounting for the possible heterogeneity of the CO adsorption sites as a function of the ring system hosting the cation. In detail, two sites, placed respectively in a large and a small ring, were investigated herein. Nomenclature and sites labelling used hereafter for defining the ring-systems refers to that proposed by the International Zeolites Association on the Database of Zeolite Structures [44]. For CHA, Cu^+ was positioned in the 6-membered ring (-MR) of the *d6r* cage or within the 8-MR window of the *cha* cage, maintaining the same position for the framework Al that is charge-balanced by the extraframework ion. The same strategy was adopted for MOR, where Al was placed in the T4 crystallographic site and the Cu^+ inside the 8-MR "side pocket" or in the 12-MR main channel. Finally, MFI models were adapted from previous report by the authors [25], with Cu^+ located near an Al positioned in the T8 site (Cu^+ in a 6-MR on channel wall) or in the T10 site (Cu^+ exposed on a 10-MR ring at channels intersection). The local structure of Cu^+ in each model is shown in Fig. 1.

The calculations were carried out with parameters from a previous work involving Cu-MFI, i.e., the hybrid GGA B3LYP functional [45,46]. Dispersive interaction have been included empirically through the Grimme D3 scheme [47]. The basis set by Nada et al. was adopted for describing Si and O atoms [48], whereas that by Catti et al. [49] was used in for Al. Extraframework Cu cations and atoms belonging to sorbed carbon monoxide (C and O) have been described by the Ahlrichs TZVP basis [50]. The truncations for the mono- and bi-electronic integral (TOLINTEG) were set to {7 7 7 7 25}. The sampling in the reciprocal space (SHRINK) was set to {2 2} ({3 3} for CHA), providing a total of 8 k points sampled in MFI and MOR (14 in CHA). The maximum order of shell multipoles in the long-range zone for the electron-electron Coulomb interaction (POLEORDR keyword) was chosen to be 6. All the other parameters were set to default values according to the CRYSTAL17 manual [51].

Each Cu^+ model was geometry optimized, then molecular adducts with carbon monoxide (mono- and di-carbonyls) were built and further optimized. The periodic models are provided in Appendix A of SI in cif format. Finally, the thermodynamic functions describing the Cu adducts (enthalpies and Gibbs free energies) were evaluated by computing harmonic frequencies over a subset of atoms including: the Cu^+ cation; the sorbed molecule(s); the Al framework atom and its neighbours up to
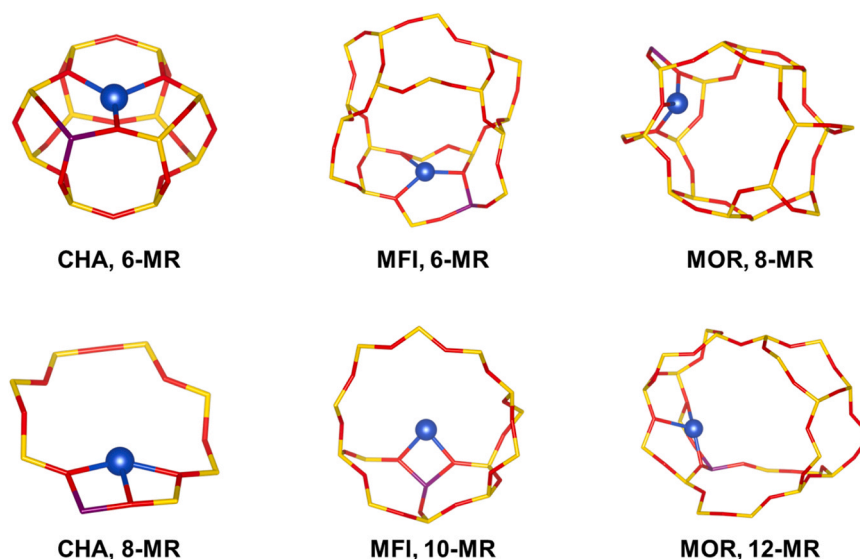

Fig. 1. Representation of the local structure of Cu^+ models considered in this work. Atoms colour code: red, O; purple, Al, yellow, Si; blue, Cu.

the 2nd coordination shell (namely 4 O and 4 Si atoms, possibly including additional atoms to fully include small 4-MR rings, if applicable).

The variation of electronic energy (ΔE), enthalpy (ΔH) and Gibbs free energy (ΔG) associated to the formation of an adduct, evaluated at experimentally relevant p,T conditions, were computed as it follows:

$$\Delta X = \sum X_{products} - \sum X_{reagents}, \text{ with } X = E, H \text{ or } G$$

3. Results and discussion

3.1. Effect of topology and composition on stationary states

X-ray spectroscopy has been extensively used as a tool to study Cu-exchanged zeolites, due to its unique ability to probe the electronic and geometric structure of the Cu sites in an element selective fashion. *In situ* and *operando* experiments are more and more practicable, and general trends and features can be described in operating conditions with good time resolution. XAS spectra in both the XANES and EXAFS regions were collected during the whole treatment for all samples. For the sake of brevity, only the XANES spectra corresponding to the stationary states for each reaction step are described in the following. Fig. 2 (left panel) shows the materials after exposure to O_2 at 500 °C. The well-known features of oxidized Cu-zeolites are present for all samples in a very similar way, namely the Cu^{2+} 1 s→3d and 1 s→4p transitions at ca. 8978 and 8987 eV, respectively, as well as the high intensity of the white line. After exposure to NH_3 (Fig. 2, central panel), the Cu^{2+} 1 s→3d transition vanishes and an intense feature at 8983 eV, corresponding to the Cu^+ 1 s→4p transition, appears. In agreement with the literature, and as confirmed by MCR-ALS (vide infra), the shape of the spectra for all materials are consistent with the presence of a major fraction of 2-coordinated Cu^+ species; in particular, the formation of $[Cu(NH_3)_2]^+$ linear complexes has been described in similar conditions for related samples. [3] Interestingly, the Cu-CHA samples show differences in the rising edge region compared to the other materials; (0.35)Cu-CHA(5) in particular shows a lower intensity of the Cu^+ 1 s→4p transition and a structured white line. This could be indicative of a lower amount of Cu^+

involved in the formation of $[Cu(NH_3)_2]^+$ complexes or, alternatively, in a distorted geometry of such complexes due to framework/composition-dependent steric constraints. After NH_3 is removed at the same temperature (Fig. 2, right panel), the spectra of the materials change and group in correspondence to the topology. In both Cu-CHA samples the intensity of the Cu^+ 1 s→4p transition decreases and the rising edge/white line region is severely modified; this seems to imply a significative structural modification of the Cu sites after NH_3 is removed. Nonetheless, also referring to previous literature, the different resulting spectrum (with respect to the other frameworks) does not infer the over-reduction of Cu to the metallic state. In fact, both the XANES and the corresponding EXAFS spectra for Cu-CHA samples does not exhibit common features with those of a reference Cu metal foil, as reported in Fig. S3. A decrease in the Cu^+ 1 s→4p transition intensity also occurs for the Cu-MFI samples, with only a slight modification in the white line region; the spectra of the Cu-MOR materials are the least affected by the removal of NH_3. The variation upon flushing with He could be rationalized in terms of the calculated structure for the framework-coordinated Cu^+ sites shown in Fig. 1: in particular, for both Cu-MOR sites the metal is ligated in a quasi-linear fashion by two of the coordinated oxygen atoms compared to the other frameworks, which would lead to an enhanced intensity of the 1 s→4p transition. For the sake of brevity, MCR-ALS decomposition of this part of the reaction is reported in the SI (Figs. S4 and S5). The NH_3 desorption rate for the three materials follows the order CHA> >MOR>MFI (from faster to slower) as retrieved from MCR-ALS decomposition (Fig. S6). This trend is likely induced by the small cage structure of the CHA topology: diffusion problems can be excluded due to the small kinetic diameter of NH_3. [52].

Upon cooling down to 50 °C, all samples retain a similar spectral shape, as shown in Fig. 3 (left panel), though the white line region for both Cu-CHA samples is slightly modified again; this peculiar behaviour could be related to the possibility of the Cu atoms to move from their initial equilibrium positions inside the zeolitic host upon interaction with NH_3, as suggested in the recent literature. [53,54] The central panel of Fig. 3 shows the interaction of CO with the samples at the same temperature. The interaction is very quick, as it will be described in
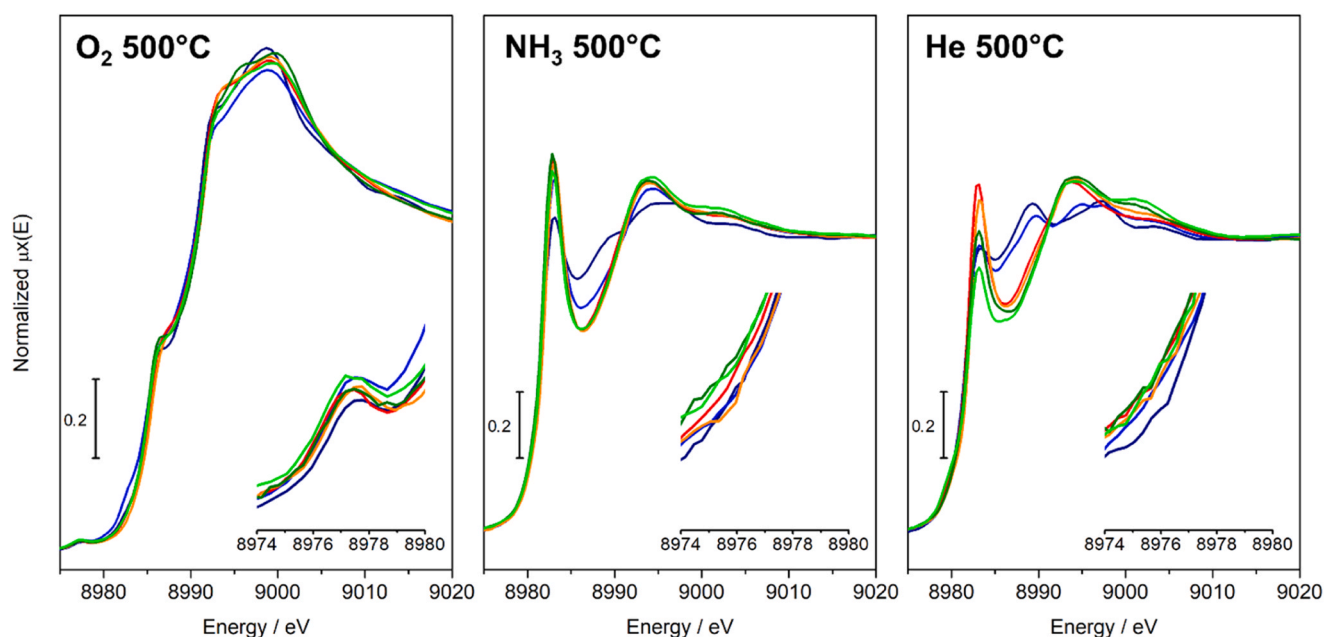

Fig. 2. Cu K-edge XANES spectra for the six Cu-zeolite samples at key reaction steps (500 °C). Insets: zoom on the 1 s-3d transition zone of the edge. Left panel: oxidized in O_2 at 500 °C. Middle panel: reduced in NH_3 at 500 °C after oxidation and He flush. Right panel: flushed with He at 500 °C after reduction in NH_3. Colour code: blue, (0.48)Cu-CHA(15); navy, (0.35)Cu-CHA(5); red, (0.32)Cu-MOR(11); orange, (0.21)Cu-MOR(6.5); light green, (0.48)Cu-MFI(25); olive, (0.35)Cu-MFI(11.5).
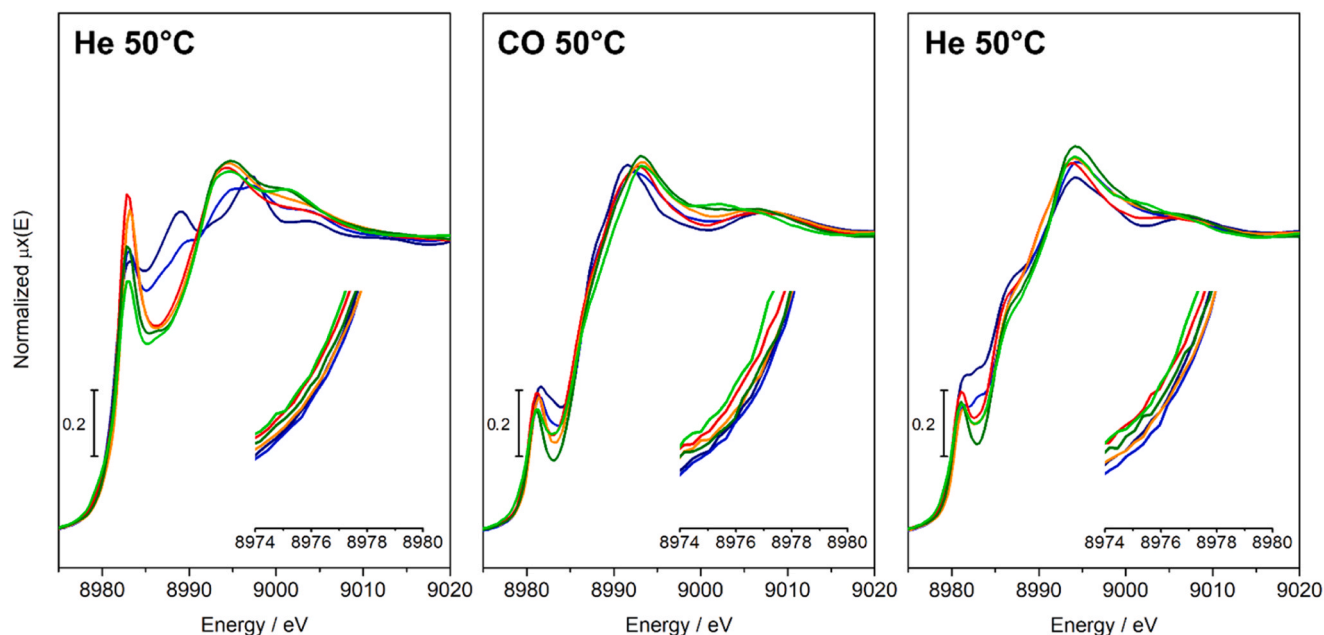
Fig. 3. Cu K-edge XANES spectra for the six Cu-zeolite samples at key reaction steps (50 °C). Insets: zoom on the 1 s-3d transition zone of the edge. Left panel: flushed in He and cooled at 50 °C. Middle panel: exposed to CO at 50 °C. Right panel: flushed with He at 50 °C after exposure to CO. Colour code: blue, (0.48)Cu-CHA(15); navy, (0.35)Cu-CHA(5); red, (0.32)Cu-MOR(11); orange, (0.21)Cu-MOR(6.5); light green, (0.48)Cu-MFI(25); olive, (0.35)Cu-MFI(11.5).

detail in the next section, and the spectral profiles drastically change leading to a similar shape for all materials. The Cu^+ 1 s→4p transition dramatically decreases, and a sharp feature at ca. 8981 eV appears, together with a shoulder on the rising edge at ca. 8987 eV. After the CO is removed from the cell by flushing with He, the spectra reach a new equilibrium as shown in Fig. 3 (right panel). In these conditions the peak at 8987 eV becomes more evident, and the feature at 8981 eV decreases in intensity for some samples (mainly the Cu-CHAs) with a simultaneous partial recovery of the Cu^+ 1 s→4p transition. A key point is that the spectral profiles of the samples after a prolonged He flushing do not correspond to those before exposure to CO; this is in agreement with the formation of at least a fraction of irreversible adducts between the Cu^+ sites and the carbon monoxide. According to the literature [28,29, 55–57], and as shown by our group in a recent publication for Cu-MFI zeolites [25], interaction of CO at 50 °C with Cu sites in the zeolitic host leads to the formation of a series of carbonyl complexes (i.e., [Cu(CO)$_2$]$^+$, [Cu(CO)]$^+$ and [Cu(CO)]$^{2+}$). When the CO partial pressure is lowered (e.g., when vacuum is applied/CO is removed from the gaseous feed) the only stable species are the Cu^+ monocarbonyls; in the case of Cu-MFI samples, [Cu(CO)]$^+$ accounted for up to 89% of total Cu species, according to volumetric measurements. A reasonable explanation for the spectral sequence shown in Fig. 3 is then the formation of multiple carbonyl species upon exposure to CO at relatively high partial pressure, followed by a partial decomplexation when the CO partial pressure is set to zero, i.e., during He flushing; the only carbonyl complex that is retained after this step is [Cu(CO)]$^+$ (i.e., the Cu^+ monocarbonyl), while a fraction of the total Cu may still be present as Cu^+ or Cu^{2+} sites co-ordinated to the framework. This picture is further confirmed by calculations and MCR analysis (vide infra). Interestingly, the peak at 8983 eV corresponding to the Cu^+ 1 s→4p transition that is partially restored after flushing likely corresponds to a fraction of Cu^+ not coordinated by CO; this seems to happen more prominently for the CHA topology, and this transition is in fact partly visible for (0.35)Cu-CHA(5), even in the presence of CO in gas phase. Since the Cu^+ 1 s→4p peak only partially overlaps with the characteristic transitions of CO-bound Cu^+ (i.e., the ones at 8981 and 8987 eV), it can be fortuitously used to qualitatively and semi-quantitatively assess the amount of Cu^+ that is not coordinated by CO. From the spectra portrayed in Fig. 3 (right

panel), the trend seems to be CHA>MOR>MFI in decreasing order of untitrated Cu^+, in good agreement with volumetric data on the same series of samples reported in Table 2.

Finally, all materials were heated up to 500 °C in He flow to study the desorption behaviour of CO and its influence on the Cu sites: the XANES spectra of all materials at the final point of this treatment are reported in Fig. 4. Though a more detailed discussion of the transient states will be presented in the next section, it is already apparent that the majority of Cu in this stationary state is present as Cu^+ species; in fact, a comparison with the spectra of the samples in He at 500 °C after treatment in NH_3 (see Fig. 2) confirms a striking similarity between the two situations. Specific differences on the samples may be due to residual [Cu(NH$_3$)$_2$]$^+$ complexes in the latter (which present a more intense Cu^+ 1 s→4p transition, as already discussed) or a slightly different positioning of the Cu sites in the two cases. This information, together with the MCR profiles presented in the next section, suggest that the [Cu(CO)]$^+$ complexes simply decompose to framework-bound Cu^+ and gaseous CO after thermal treatment; this phenomenon can thus be described as a simple desorption and does not involve a change of Cu oxidation state nor a decomposition of CO.

3.2. Quantitative analysis using MCR-ALS

Fig. 5 portrays the MCR-ALS reconstruction on the spectral series shown in Fig. 3 consisting of the steps at 50 °C for an example material for each framework, namely (0.35)Cu-CHA(5), (0.32)Cu-MOR(11) and (0.35)Cu-MFI(11.5); the same reconstruction for the other materials is reported in Fig. S7. The spectra extracted for the 3 identified components are consistent with a bare Cu^+ species, a Cu^+ dicarbonyl and a Cu^+ monocarbonyl adduct. As already discussed in the previous section, the

Table 2
Cu^+ concentrations measured by isothermal volumetric adsorption of CO at 50 °C on the 3 samples discussed in the previous section.

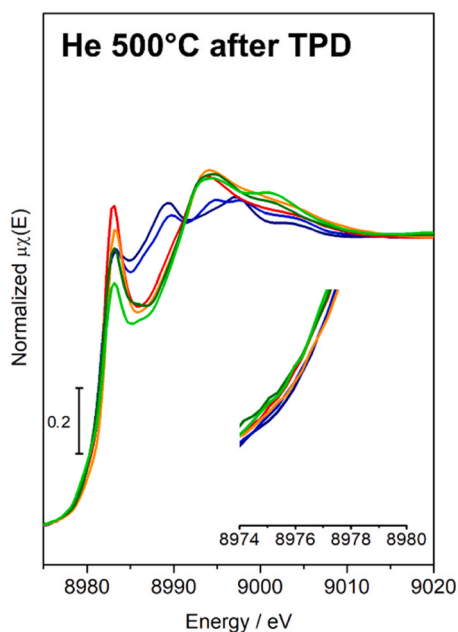| Sample	CO uptake (mmol/g)	Cu^+ concentration (%)
(0.35)Cu-CHA(5)	0.480	60.6
(0.32)Cu-MOR(11)	0.322	74.6
(0.35)Cu-MFI(11.5)	0.401	89.1

Fig. 4. Cu K-edge XANES spectra for the six Cu-zeolite samples at 500 °C after temperature programmed desorption of CO in He. Inset: zoom on the 1 s-3d transition zone of the edge. Colour code: blue, (0.48)Cu-CHA(15); navy, (0.35) Cu-CHA(5); red, (0.32)Cu-MOR(11); orange, (0.21)Cu-MOR(6.5); light green, (0.48)Cu-MFI(25); olive, (0.35)Cu-MFI(11.5).

spectrum of the bare Cu^+ is characterized by an intense pre-edge 1 s→4p transition centred at 8983 eV and by an unstructured white line of comparable intensity (except in the case of Cu-CHA). This spectral shape nicely matches the PC1 component shown in Fig. 5. PC2 presents its higher concentration when CO is present at high partial pressure in the gaseous feed, thus can be reasonably assigned to a high-coverage situation, i.e. to the formation of $[Cu(CO)_2]^+$ adducts. Finally, PC3 is consistent with the presence of $[Cu(CO)]^+$ adducts, as it is found to be stable at 50 °C under a negligible CO partial pressure, as expected from previous reports. Interestingly, though the shape of the white line region for the CHA topology is again confirmed, the spectra of the carbonyl adducts are similar across the three framework types. This fact suggests a lower involvement of the zeolitic framework in determining the local structure of the Cu-carbonyl adducts. Although some error stemming from the algorithm is to be expected, useful information about the relative proportion of the species can be extracted from the concentration profiles (bottom panels of Fig. 5). In all cases, the conversion from bare Cu^+ to $[Cu(CO)_2]^+$ adducts is quantitative, but for the CHA topology a complete formation of $[Cu(CO)]^+$ species after flushing He is never achieved: the conversion of $[Cu(CO)_2]^+$ to $[Cu(CO)]^+$ is not quantitative for (0.35)Cu-CHA(5) (c.a. 95%) and is readily accompanied by the formation of a fraction of bare Cu^+ species (c.a. 5% for CHA samples) in less than 45 min, in agreement with what was previously described (vide supra). The reversibility of these adducts is observed also for the other materials, but it appears to be enhanced for the CHA topology, possibly due to the steric constraints imposed by the small cage system (and the relative abundance of Cu for the (0.35)Cu-CHA(5) material). In the case of (0.35)Cu-CHA(5) the desorption was registered for a longer time during the experiment (full range in Fig. S8), and the MCR concentration profile shows a very clean distinction between the different species with almost 10% of residual unbound Cu^+ species after 65 min.

The MCR-ALS reconstruction performed on the TPD step is shown in Fig. 6 for the selected samples; the reconstruction for the other samples is reported in Fig. S9. In this case, although not immediately evident from the experimental spectra, 3 components are retrieved for all

materials. From the concentration profiles (bottom panels in Fig. 6), it is apparent that the initial monocarbonyl species first convert to an intermediate species at lower temperatures, which then yields the final species upon further heating. Since the final state highly resembles the spectrum of the reduced material at 500 °C after NH_3 removal, the intermediate state is probably indicative of a bare Cu^+ species bound to the framework in a different equilibrium position than the one at 500 °C. For the MOR and MFI framework, this species bears a striking similarity to the bare Cu^+ species at 50 °C shown in Fig. 3 (left panel), so the spectral series can be described in terms of two subsequent events: the thermally-induced desorption of CO from the $[Cu(CO)]^+$ complex, leading to the formation of a low-temperature bare Cu^+ species reaching maximum concentration at ca. 300 °C, and the geometrical rearrangement of this species at higher temperatures. In the case of CHA, however, the intermediate state resembles more the intermediates of the other framework than the state before exposure to CO in Fig. 3 (right panel); a possible explanation for this difference is a mobilization of the Cu in the CHA framework due to treatment in NH_3, with a subsequent repositioning after interaction with CO and/or thermal treatment. This species is also formed at lower temperatures compared to the other frameworks, and reaches maximum concentration at a temperature of ca. 250 °C and 150 °C for (0.48)Cu-CHA(15) and (0.35)Cu-CHA(5), respectively. An overall lower thermal stability of Cu-carbonyls in the CHA framework is in accordance with DFT calculations (vide infra), and is already apparent from the presence of ca. 10% of the intermediate species at the starting point of the TPD for (0.35)Cu-CHA(5). It has to be noted, though, that the Cu density in the framework for (0.35)Cu-CHA(5) is higher compared to the MOR and MFI samples (0.87 compared to 0.47 and 0.45, respectively), so that concentration-dependent effects may also play a role in such a striking difference. Still, the same method applied to the (0.48)Cu-CHA(15) sample (with a 0.45 Cu density) yields a maximum for the formation of the low-temperature Cu^+ species at 250 °C, still lower than all other non-CHA samples. Together with the peculiar speciation of Cu^+ species in the CHA framework and the results from DFT calculations (vide infra), framework-dependent properties (especially in the case of CHA) appear to play the major role in this case.

3.3. Isothermal volumetric CO adsorption

Results for isothermal volumetric CO adsorption measurements on the samples described in the previous sections are reported in Table 2 (full isotherms shown in Fig. S10). The amount of Cu^+ measured on the samples is in line with the results obtained via MCR-ALS, showing a slow, but measurable, decomposition of the $[Cu(CO)]^+$ adducts over time in the order CHA> >MOR>MFI. The longer desorption times employed during the volumetric experiments, compared to the XAS measurements, can justify the lower amounts of Cu^+ computed by this experimental tool, especially for the CHA topology, where the presence of a significant fraction of uncoordinated Cu^+ is already observable in the spectra (Fig. 3, right panel). The lower stability of the $[Cu(CO)]^+$ adducts in the CHA framework was also confirmed by DFT calculation, as shown in the next section.

3.4. Insights from simulation

The formation of $[Cu(CO)_2]^+$ adducts on Cu^+ at 50 °C in the presence of CO and the subsequent decomposition to $[Cu(CO)]^+$ when the CO partial pressure is decreased were observed for all the investigated samples; specific differences were found depending on the framework type, and especially in the case of CHA, the monocarbonyl complex appeared to be less stable than in the other topologies. In the view of getting an atomistic description of the adsorption/desorption processes, DFT simulations were performed on a set of representative structures for each topology investigated in this work. As shown in Fig. 1, depending on the framework topology/ring structure where Cu^+ is sitting, various coordination geometries are possible for the ion toward the framework.
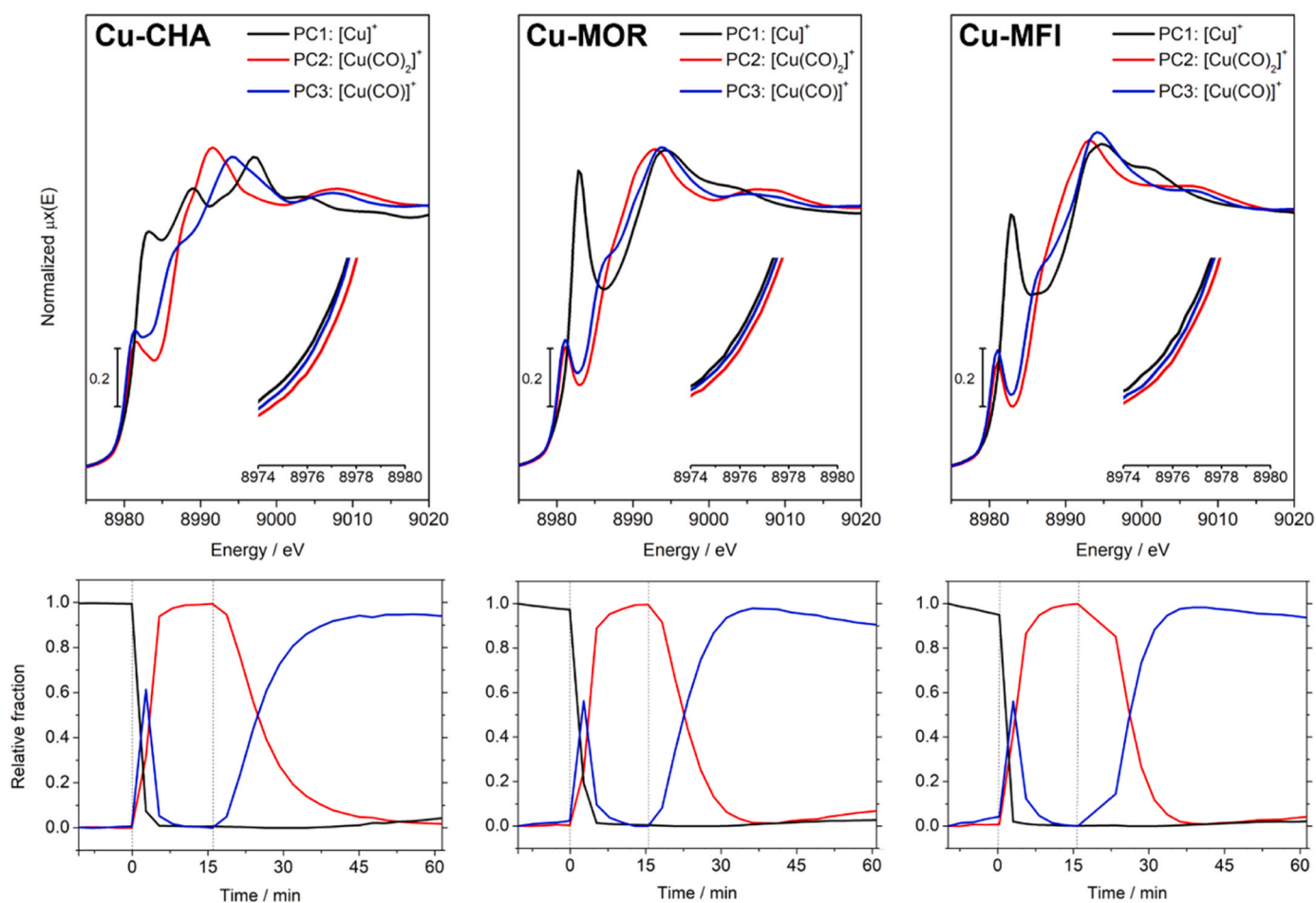
Fig. 5. Pure spectral (top) and concentration (bottom) profiles extracted by MCR-ALS on a sample of each framework type during the steps at 50 °C described in Fig. 3 (vide supra). Insets: zoom on the 1 s-3d transition zone of the edge. Colour code: black, Cu^+ coordinated to the framework; red, $[Cu(CO)_2]^+$ complex coordinated to the framework; blue, $[Cu(CO)]^+$ complex coordinated to the framework.

The main coordination motifs can be identified are: i) a T-shaped geometry, with Cu^+ bridging across two equidistant framework O atoms, with the contribution of a third framework O at slightly longer distance, typical of Cu^+ sitting in large pores; ii) a trigonal geometry, with Cu^+ coordinated by three closely equivalent framework O atoms, observed in smaller pores/more constrained cavities. An exception to this trend is represented by Cu^+ positioned in the 10-MR of MFI, grafted to two non-collinear, Al-bound O framework atoms. Upon interaction with the first CO molecule (see graphical representation of optimized structures in Figs. S11-*13*), regardless the considered Cu^+ site, the adsorption event causes the detachment of the metal ion from the framework, now assuming a quasi-trigonal coordination with two framework O and the C atom from the adsorbate. The adsorption of a second CO molecule expands the Cu^+ coordination sphere to a quasi-tetrahedral one, with the only exception of the Cu^+ site hosted in the 8-MR that is unable to coordinate a second CO molecule, as due to the steric constraint imposed by the confined environment in the MOR side pocket.

Table 3 lists the electronic energy, enthalpy and Gibbs free energy variations computed for the formation of $[Cu(CO)]^+$ and $[Cu(CO)_2]^+$ adducts starting from a bare Cu^+ site in different positions inside each framework.

In all cases, the formation of the carbonyl adducts is thermodynamically favoured (except for the $[Cu(CO)_2]^+$ in the 8-membered ring for the MOR topology, that is not formed in practice). Both in terms of enthalpy and Gibbs free energy, the MFI topology shows the highest stability among the series for the formation of $[Cu(CO)]^+$ adducts, consistently with experimental observations. On the other hand, the

CHA framework presents the lowest difference in energies between the mono- and dicarbonyl species, as well as the highest energy (-38.6 kJ/mol) for the $[Cu(CO)]^+$ adduct in the 6-membered ring position. This difference is likely the reason for the strikingly different behaviour of the samples of this topology (especially (0.35)Cu-CHA(5)) upon prolonged CO desorption.

Finally, calculated phase diagrams showing the stability of $[Cu(CO)_2]^+$ and $[Cu(CO)_2]^+$ adducts as a function of temperature and pressure are portrayed in Fig. 7.

Although the pressure gauge in the volumetric instrument can accurately read pressure down to 10^{-3} mbar (which has been used as the lower bound for the phase diagrams), the actual pressure in the sample cell is likely to be lower than this value since a turbomolecular pump is used to evacuate the cell; this is also consistent with the MCR reconstruction, in which no evidence of residual Cu-dicarbonyls (except in the case of Cu-CHA) is found. As can be observed, the average temperature for the decomposition of the $[Cu(CO)]^+$ to a bare Cu^+ species at 10^{-3} mbar (that well approximates a negligible partial pressure of CO in flow experiments) in the case of CHA (162 °C) is much lower than that for the other two frameworks (275 °C and 340 °C for MOR and MFI, respectively), especially in the case of Cu located in the 6-membered rings. Supposing an unequal occupancy of the Cu sites in the different rings, the trend in terms of framework topology is still respected. These average temperatures are in perfect agreement with what was found from MCR-ALS during the TPD steps for the three samples (see Fig. 6, bottom panels) confirming the general trend in desorption kinetics and overall stability for the three topologies.
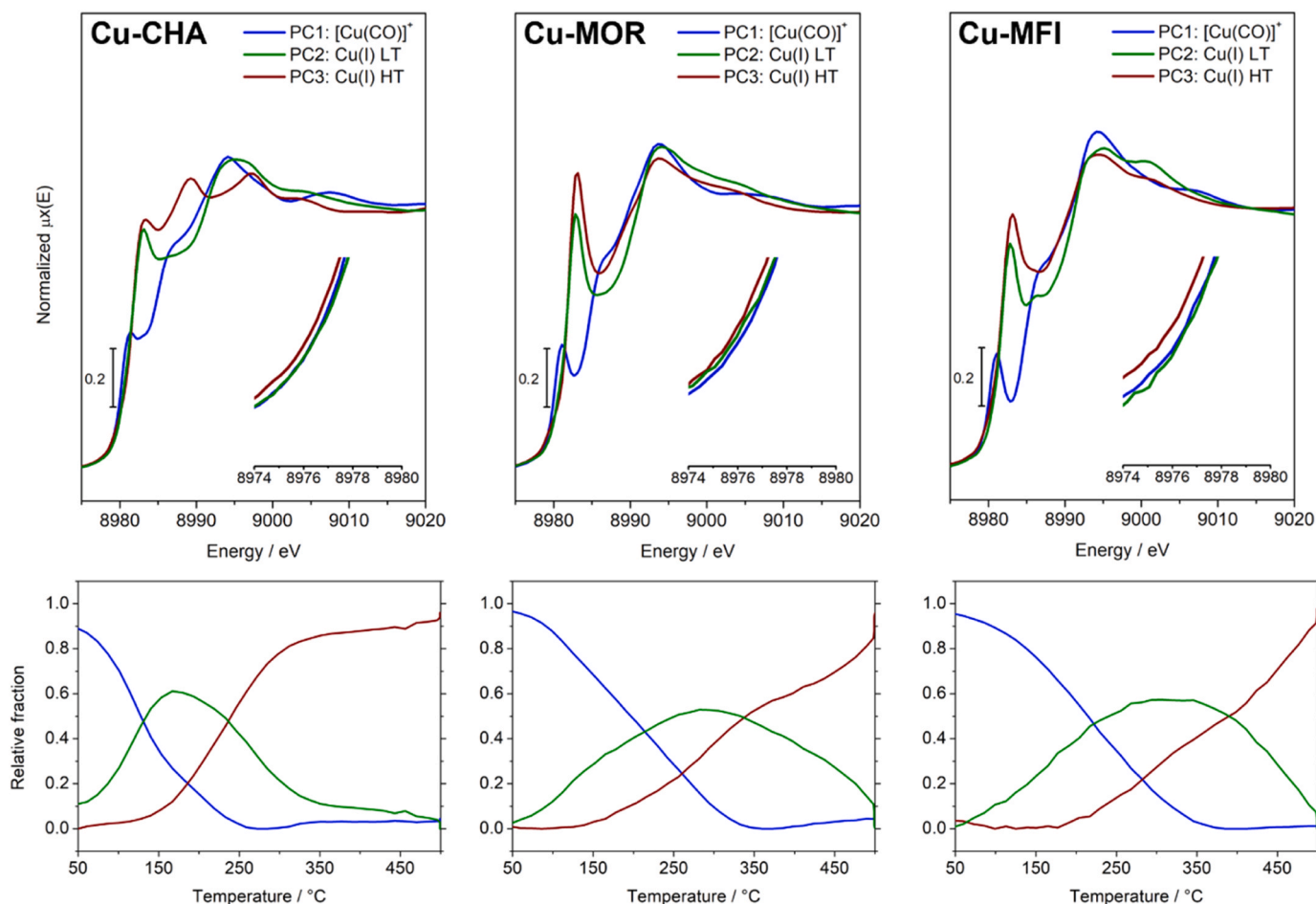
Fig. 6. Pure spectral (top) and concentration (bottom) profiles extracted by MCR-ALS on a sample of each framework type during the TPD procedure (vide supra). Insets: zoom on the 1 s-3d transition zone of the edge. Colour code: blue, $[Cu(CO)]^+$ complex coordinated to the framework; olive, Cu^+ species at lower temperatures (LT); wine, Cu^+ species at higher temperatures (HT).

Table 3
Electronic energies (ΔE), enthalpies (ΔH) and Gibbs free energies (ΔG) variations associated to the formation of mono- and di-carbonyl molecular adducts on Cu^+, located at different positions within the CHA, MFI and MOR frameworks. All values are reported in kJ/mol. ΔH and ΔG computed at 25 °C and 1013 mbar.

			ΔE	ΔH	ΔG	ΔE	ΔH	ΔG
			6-MR			8-MR		
CHA		$[Cu(CO)]^+$	-83.8	-78.2	-38.6	-143.0	-121.8	-76.6
		$[Cu(CO)_2]^+$	-56.7	-51.6	-10.4	-75.2	-81.2	-40.3
			6-MR			10-MR		
MFI		$[Cu(CO)]^+$	-125.7	-119.2	-78.7	-169.3	-163.3	-121.0
		$[Cu(CO)_2]^+$	-51.0	-46.0	-8.9	-65.8	-63.7	-19.7
			8-MR			12-MR		
MOR		$[Cu(CO)]^+$	-121.4	-118.8	-72.3	-112.1	-111.3	-75.9
		$[Cu(CO)]^+ + CO$	-29.3	-22.5	7.6	-68.1	-62.9	-20.4

4. Conclusions

A pool of Cu-exchanged zeolites, bearing different topology and composition, has been systematically investigated after a high temperature reduction protocol in NH_3 to quantify the amount of Cu involved in the reduction to Cu^+. Subsequently, interaction with CO at 50 °C and its desorption upon heating was investigated. MCR-assisted time-resolved XAS spectroscopy is consistent with a quantitative reduction for all studied materials, with a different spectral behaviour in the specific case of CHA. Interaction with CO at lower temperature promotes the formation of $[Cu(CO)_2]^+$ complexes, that easily decompose to $[Cu(CO)]^+$ upon flushing with inert. Once formed, the latter adducts are stable with the exception of CHA, which shows a very slow but measurable decomposition to Cu^+ and CO. In all cases, thermal treatment up to 500 °C in inert promotes the desorption of CO to form two different bare Cu^+ species depending on the temperature. For CHA, the low temperature species is different compared to the one obtained by reducing the sample and cooling it down; this new species is more similar to the ones obtained for the other samples, and it is likely related to a different geometric arrangement inside the CHA pores. Isothermal volumetric CO adsorption measurements at 50 °C were in agreement with the results found by XAS: although it is more affected by the CO desorption kinetics, this indirect methodology allows Cu^+ quantitative assessment without the necessity for large scale facility applications. The particular
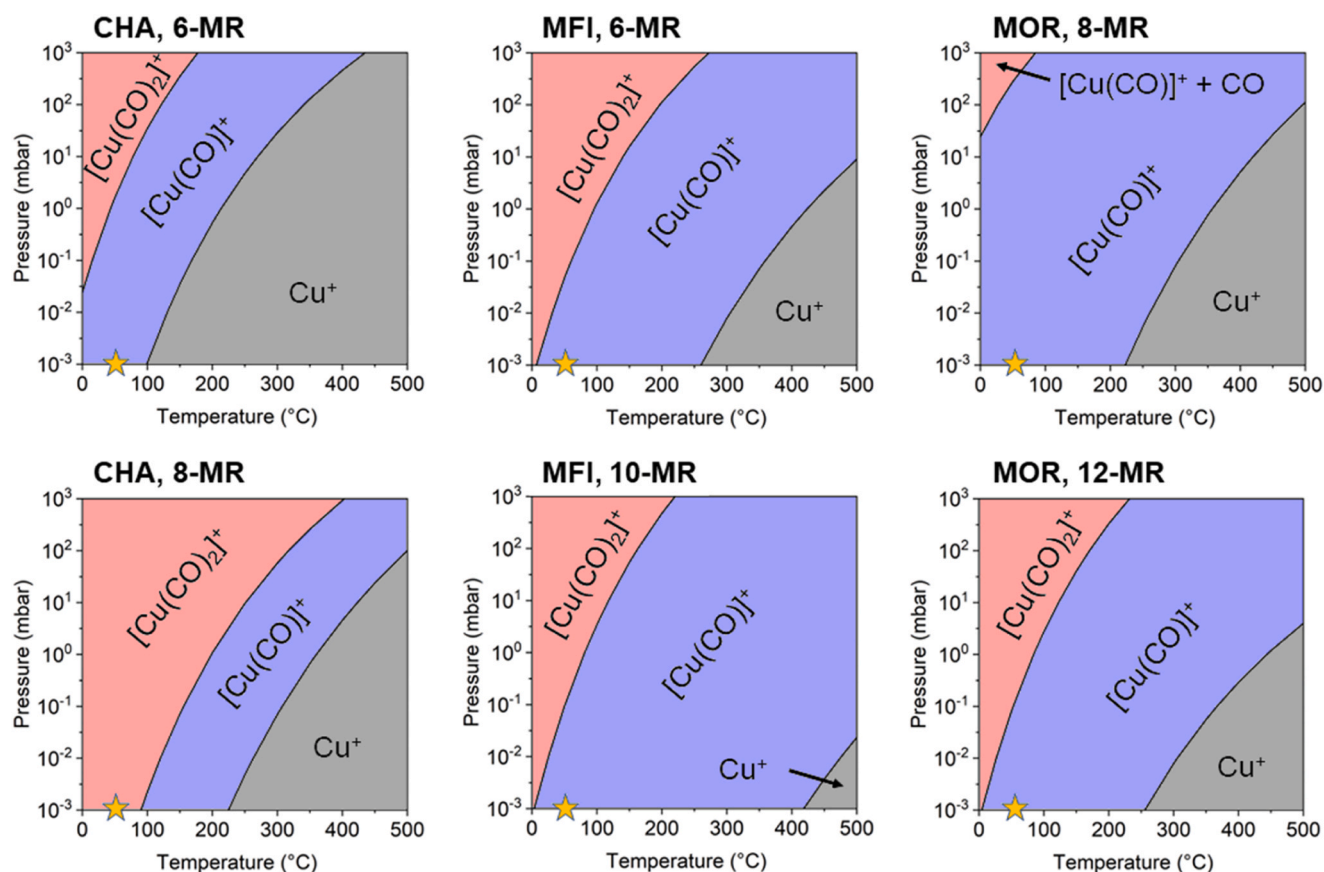
Fig. 7. Phase diagrams depicting the relative stabilities of isolated Cu^+, $[Cu(CO)]^+$ and $[Cu(CO)_2]^+$ as a function of temperature and pressure, for each structural model considered in this work. Yellow stars label the condition at which Cu^+ content is evaluated via monocarbonyls titration in the volumetric measurement. As can be seen in the top-right panel, no stable dicarbonyl adducts are found in the case of the 8-MR in MOR (labelled as $[Cu(CO)]^+ + CO$).

behaviour of CHA was studied by periodic DFT calculations and compared to properties of the other frameworks, confirming the lower stability of the carbonyl adducts for this framework; calculation of state diagrams highlighted as the dependence on the temperature and CO partial pressure were in agreement with the trends retrieved during temperature-dependent desorption analysed by MCR, with specific differences depending on the Cu siting within the different frameworks.

CRediT authorship contribution statement

Gabriele Deplano: Conceptualization; Methodology; Formal analysis; Writing – original draft; Writing – review & editing; Visualization; Investigation. **Matteo Signorile**: Conceptualization; Methodology; Data curation; Writing – original draft; Writing – review & editing; Visualization; Investigation; Supervision. **Cesare Atzori**: Methodology; Investigation. **Davide Salusso**:Investigation. **Elisa Borfecchia**: Conceptualization; Supervision. **Valentina Crocellà**: Methodology; Investigation; Supervision. **Silvia Bordiga**: Conceptualization; Supervision; Project administration Funding acquisition.

Declaration of Competing Interest

The authors declare that they have no known competing financial interests or personal relationships that could have appeared to influence the work reported in this paper.

Data availability

Data will be made available on request.

Appendix A. Supporting information

Supplementary data associated with this article can be found in the online version at doi:10.1016/j.cattod.2023.114403.

References

[1] M.A. Newton, A.J. Knorpp, V.L. Sushkevich, D. Palagin, J.A. van Bokhoven, Active sites and mechanisms in the direct conversion of methane to methanol using Cu in zeolitic hosts: a critical examination, Chem. Soc. Rev. (2020), https://doi.org/10.1039/c7cs00709d.
[2] S. Mohan, P. Dinesha, S. Kumar, NOx reduction behaviour in copper zeolite catalysts for ammonia SCR systems: a review, Chem. Eng. J. (2020) *384*, https://doi.org/10.1016/j.cej.2019.123253.
[3] E. Borfecchia, P. Beato, S. Svelle, U. Olsbye, C. Lamberti, S. Bordiga, Cu-CHA-a model system for applied selective redox catalysis, Chem. Soc. Rev. 47 (22) (2018) 8097–8133, https://doi.org/10.1039/c8cs00373d.

[4] V.F. Kispersky, A.J. Kropf, F.H. Ribeiro, J.T. Miller, Low absorption vitreous carbon reactors for operando XAS: a case study on Cu/zeolites for selective catalytic reduction of NOx by NH3, Phys. Chem. Chem. Phys. 14 (7) (2012) 2229–2238, https://doi.org/10.1039/c1cp22992c.

[5] S.H. Krishna, C.B. Jones, J.T. Miller, F.H. Ribeiro, R. Gounder, Combining kinetics and operando spectroscopy to interrogate the mechanism and active site requirements of NOx selective catalytic reduction with NH3 on Cu-zeolites, J. Phys. Chem. Lett. 11 (13) (2020) 5029–5036, https://doi.org/10.1021/acs.jpclett.0c00903.

[6] L. Negahdar, N.E. Omori, M.G. Quesne, M.D. Frogley, F. Cacho-Nerin, W. Jones, S. W.T. Price, C.R.A. Catlow, A.M. Beale, Elucidating the significance of copper and nitrate speciation in Cu-SSZ-13 for N2O formation during NH3-SCR, ACS Catal. 11 (21) (2021) 13091–13101, https://doi.org/10.1021/acscatal.1c03174.

[7] S.H. Krishna, A. Goswami, Y.J. Wang, C.B. Jones, D.P. Dean, J.T. Miller, W. F. Schneider, R. Gounder, Influence of framework Al density in chabazite zeolites on copper ion mobility and reactivity during NOx selective catalytic reduction with NH3, Nat. Catal. 6 (3) (2023) 276–285, https://doi.org/10.1038/s41929-023-00932-5.

[8] K. Kvande, D.K. Pappas, E. Borfecchia, K.A. Lomachenko, Advanced X-ray absorption spectroscopy analysis to determine structure-activity relationships for Cu-zeolites in the direct conversion of methane to methanol, ChemCatChem 12 (9) (2020) 2385–2405, https://doi.org/10.1002/cctc.201902371.

[9] G. Berlier, V. Crocellà, M. Signorile, E. Borfecchia, F. Bonino, S. Bordiga, Characterization of Metal Centers in Zeolites for Partial Oxidation Reactions. In *STRUCTURE AND REACTIVITY OF METALS IN ZEOLITE*, in: J.P. Pariente, M. SanchezSanchez (Eds.), Materials, Vol. 178, 2018, pp. 91–154, https://doi.org/10.1007/430_2018_24.

[10] M. Mao, L.M. Liu, Z.H. Liu, Recent insights into Cu-based catalytic sites for the direct conversion of methane to methanol, Molecules 27 (21) (2022), https://doi.org/10.3390/molecules27217146.

[11] J.L. Chen, W. Huang, S.Z. Bao, W.B. Zhang, T.Y. Liang, S.K. Zheng, L. Yi, L. Guo, X. Q. Wu, A review on the characterization of metal active sites over Cu-based and Fe-based zeolites for NH3-SCR, RSC Adv. 12 (43) (2022) 27746–27765, https://doi.org/10.1039/d2ra05107a.

[12] B. Guan, H. Jiang, Y. Wei, Z. Liu, X. Wu, H. Lin, Z. Huang, Density functional theory researches for atomic structure, properties prediction, and rational design of selective catalytic reduction catalysts: current progresses and future perspectives, Mol. Catal. 510 (2021), 111704, https://doi.org/10.1016/j.mcat.2021.111704.

[13] E. Broclawik, P. Kozyra, M. Mitoraj, M. Radoń, P. Rejmak, Zeolites at the molecular level: what can be learned from molecular modeling, Molecules (2021), https://doi.org/10.3390/molecules26061511.

[14] M.H. Mahyuddin, Y. Shiota, A. Staykov, K. Yoshizawa, Theoretical overview of methane hydroxylation by copper–oxygen species in enzymatic and zeolitic catalysts, Acc. Chem. Res. 51 (10) (2018) 2382–2390, https://doi.org/10.1021/acs.accounts.8b00236.

[15] R. Millan, P. Cnudde, V. van Speybroeck, M. Boronat, Mobility and reactivity of Cu + species in Cu-CHA catalysts under NH3-SCR-NOx reaction conditions: insights from AIMD simulations, JACS Au 1 (10) (2021) 1778–1787, https://doi.org/10.1021/jacsau.1c00337.

[16] D.W. Fickel, R.F. Lobo, Copper coordination in Cu-SSZ-13 and Cu-SSZ-16 investigated by variable-temperature XRD, J. Phys. Chem. C. 114 (3) (2010) 1633–1640, https://doi.org/10.1021/jp9105025.

[17] U. Deka, A. Juhin, E.A. Eilertsen, H. Emerich, M.A. Green, S.T. Korhonen, B. M. Weckhuysen, A.M. Beale, Confirmation of isolated Cu2+ ions in SSZ-13 zeolite as active sites in NH3-selective catalytic reduction, J. Phys. Chem. C. 116 (7) (2012) 4809–4818, https://doi.org/10.1021/jp2450d.

[18] X. Tang, J. Ye, L. Guo, T. Pu, L. Cheng, X.-M. Cao, Y. Guo, L. Wang, Y. Guo, W. Zhan, S. Dai, Atomic insights into the Cu species supported on zeolite for direct oxidation of methane to methanol via low-damage HAADF-STEM, Adv. Mater. 35 (25) (2023) 2208504, https://doi.org/10.1002/adma.202208504.

[19] J. Song, Y. Wang, E.D. Walter, N.M. Washton, D. Mei, L. Kovarik, M.H. Engelhard, S. Prodinger, Y. Wang, C.H.F. Peden, F. Gao, Toward rational design of Cu/SSZ-13 selective catalytic reduction catalysts: implications from atomic-level understanding of hydrothermal stability, ACS Catal. 7 (12) (2017) 8214–8227, https://doi.org/10.1021/acscatal.7b03020.

[20] A.G. Greenaway, A. Marberger, A. Thetford, I. Lezcano-González, M. Agote-Arán, M. Nachtegaal, D. Ferri, O. Kröcher, C.R.A. Catlow, A.M. Beale, Detection of key transient Cu intermediates in SSZ-13 during NH3-SCR DeNOx by modulation excitation IR spectroscopy, Chem. Sci. 11 (2) (2020) 447–455, https://doi.org/10.1039/C9SC04905C.

[21] D.K. Pappas, E. Borfecchia, M. Dyballa, I.A. Pankin, K.A. Lomachenko, A. Martini, M. Signorile, S. Teketel, B. Arstad, G. Berlier, C. Lamberti, S. Bordiga, U. Olsbye, K. P. Lillerud, S. Svelle, P. Beato, Methane to methanol: structure-activity relationships for Cu-CHA, J. Am. Chem. Soc. 139 (42) (2017) 14961–14975, https://doi.org/10.1021/jacs.7b06472.

[22] A. Martini, E. Borfecchia, Spectral decomposition of X-ray absorption spectroscopy datasets: methods and applications, Crystals (2020), https://doi.org/10.3390/cryst10080664.

[23] A.A. Guda, S.A. Guda, A. Martini, A.N. Kravtsova, A. Algasov, A. Bugaev, S. P. Kubrin, L.V. Guda, P. Šot, J.A. van Bokhoven, C. Copéret, A.V. Soldatov, Understanding X-ray absorption spectra by means of descriptors and machine learning algorithms, npj Comput. Mater. 7 (1) (2021) 203, https://doi.org/10.1038/s41524-021-00664-9.

[24] C. Negri, E. Borfecchia, A. Martini, G. Deplano, K.A. Lomachenko, T.V.W. Janssens, G. Berlier, S. Bordiga, In situ X-ray absorption study of Cu species in Cu-CHA catalysts for NH3-SCR during temperature-programmed reduction in NO/NH3,

[25] Res. Chem. Intermed. 47 (1) (2021) 357–375, https://doi.org/10.1007/s11164-020-04350-1.

[25] G. Deplano, M. Signorile, V. Crocellà, N.G. Porcaro, C. Atzori, B.G. Solemsli, S. Svelle, S. Bordiga, Titration of Cu(I) sites in Cu-ZSM-5 by volumetric CO adsorption, ACS Appl. Mater. Interfaces 14 (18) (2022) 21059–21068, https://doi.org/10.1021/acsami.2c03370.

[26] C. Lamberti, S. Bordiga, M. Salvalaggio, G. Spoto, A. Zecchina, F. Geobaldo, G. Vlaic, M. Bellatreccia, I.R. XAFS, and UV−Vis study of the cui environment in CuI-ZSM-5, J. Phys. Chem. B 101 (3) (1997) 344–360, https://doi.org/10.1021/jp9601577.

[27] H. Yamashita, M. Matsuoka, K. Tsuji, Y. Shioya, M. Anpo, M. Che, In-situ XAFS, photoluminescence, and IR investigations of copper ions included within various kinds of zeolites. Structure of Cu(I) ions and their interaction with CO molecules, J. Phys. Chem. 100 (1) (1996) 397–402, https://doi.org/10.1021/jp952666z.

[28] A. Zecchina, S. Bordiga, G.T. Palomino, D. Scarano, C. Lamberti, M. Salvalaggio, Mono-, Di-, and tricarbonylic species in copper(I)-exchanged zeolite ZSM-5: comparison with homogeneous copper(I) carbonylic structures, J. Phys. Chem. B 103 (19) (1999) 3833–3844, https://doi.org/10.1021/jp9842289.

[29] S. Bordiga, G. Turnes Palomino, D. Arduino, C. Lamberti, A. Zecchina, C. Otero Areán, Well defined carbonyl complexes in Ag+- and Cu+-exchanged ZSM-5 zeolite: a comparison with homogeneous counterparts, J. Mol. Catal. A Chem. 146 (1–2) (1999) 97–106, https://doi.org/10.1016/S1381-1169(99)00082-5.

[30] T.V.W. Janssens, H. Falsig, L.F. Lundegaard, P.N.R. Vennestrøm, S.B. Rasmussen, P. G. Moses, F. Giordanino, E. Borfecchia, K.A. Lomachenko, C. Lamberti, S. Bordiga, A. Godiksen, S. Mossin, P. Beato, A consistent reaction scheme for the selective catalytic reduction of nitrogen oxides with ammonia, ACS Catal. 5 (5) (2015) 2832–2845, https://doi.org/10.1021/cs501673g.

[31] D.K. Pappas, A. Martini, M. Dyballa, K. Kvande, S. Teketel, K.A. Lomachenko, R. Baran, P. Glatzel, B. Arstad, G. Berlier, C. Lamberti, S. Bordiga, U. Olsbye, S. Svelle, P. Beato, E. Borfecchia, The nuclearity of the active site for methane to methanol conversion in Cu-mordenite: a quantitative assessment, J. Am. Chem. Soc. 140 (45) (2018) 15270–15278, https://doi.org/10.1021/jacs.8b08071.

[32] G. Deplano, A. Martini, M. Signorile, E. Borfecchia, V. Crocellà, S. Svelle, S. Bordiga, Copper pairing in the mordenite framework as a function of the CuI/cuii speciation, Angew. Chem. - Int. Ed. 60 (49) (2021) 25891–25896, https://doi.org/10.1002/anie.202109705.

[33] O. Mathon, A. Beteva, J. Borrel, D. Bugnazet, S. Gatla, R. Hino, I. Kantor, T. Mairs, M. Munoz, S. Pasternak, F. Perrin, S. Pascarelli, The time-resolved and extreme conditions XAS (TEXAS) facility at the european synchrotron radiation facility: the general-purpose EXAFS bending-magnet beamline BM23, J. Synchrotron Radiat. 22 (6) (2015) 1548–1554, https://doi.org/10.1107/S1600577515017786.

[34] https://doi.esrf.fr/10.15151/ESRF-ES-780223803.

[35] D. Bellet, B. Gorges, A. Dallery, P. Bernard, E. Pereiro, J. Baruchel, A 1300K furnace for {\it in Situ} X-ray microtomography, J. Appl. Crystallogr. 36 (2) (2003) 366–367, https://doi.org/10.1107/S0021889803001158.

[36] C. Lamberti, S. Bordiga, F. Bonino, C. Prestipino, G. Berlier, L. Capello, F. D'Acapito, F.X. i Xamena, A. Zecchina, Determination of the oxidation and coordination state of copper on different Cu-based catalysts by XANES spectroscopy in situ or in operando conditions, Phys. Chem. Chem. Phys. 5 (20) (2003) 4502–4509, https://doi.org/10.1039/B305810G.

[37] S. Bordiga, E. Groppo, G. Agostini, J.A. van Bokhoven, C. Lamberti, Reactivity of surface species in heterogeneous catalysts probed by in situ X-ray absorption techniques, Chem. Rev. 113 (3) (2013) 1736–1850, https://doi.org/10.1021/cr2000898.

[38] M. Newville, Larch: an analysis package for XAFS and related spectroscopies, J. Phys. Conf. Ser. 430 (1) (2013) 12007, https://doi.org/10.1088/1742-6596/430/1/012007.

[39] J. Jaumot, R. Gargallo, A. de Juan, R. Tauler, A graphical user-friendly interface for MCR-ALS: a new tool for multivariate curve resolution in MATLAB, Chemom. Intell. Lab. Syst. 76 (1) (2005) 101–110, https://doi.org/10.1016/j.chemolab.2004.12.007.

[40] C. Ruckebusch, Resolving Spectral Mixtures: With Applications from Ultrafast Time-Resolved Spectroscopy to Super-Resolution Imaging, Elsevier, Amsterdam, 2016.

[41] P. Conti, S. Zamponi, M. Giorgetti, M. Berrettoni, W.H. Smyrl, Multivariate curve resolution analysis for interpretation of dynamic Cu K-edge X-ray absorption spectroscopy spectra for a Cu doped V2O5 lithium battery, Anal. Chem. 82 (9) (2010) 3629–3635, https://doi.org/10.1021/ac902865h.

[42] Crocellà, V.; Atzori, C.; Latini; G.; Signorile, M. A Kit for Volumetric Measurements of Gas Adsorption. PCT/IB2021/051769, 2021.

[43] A. Erba, J. Baima, I. Bush, R. Orlando, R. Dovesi, Large-scale condensed matter DFT simulations: performance and capabilities of the crystal code, J. Chem. Theory Comput. 13 (10) (2017) 5019–5027, https://doi.org/10.1021/acs.jctc.7b00687.

[44] ⟨https://europe.iza-structure.org/IZA-SC/ftc_table.php⟩.

[45] A.D. Becke, A new mixing of hartree–fock and local density-functional theories, J. Chem. Phys. 98 (2) (1993) 1372–1377, https://doi.org/10.1063/1.464304.

[46] C. Lee, W. Yang, R.G. Parr, Development of the colle-salvetti correlation-energy formula into a functional of the electron density, Phys. Rev. B 37 (2) (1988) 785–789, https://doi.org/10.1103/PhysRevB.37.785.

[47] S. Grimme, J. Antony, S. Ehrlich, H. Krieg, A consistent and accurate ab initio parametrization of density functional dispersion correction (DFT-D) for the 94 elements H-Pu, J. Chem. Phys. 132 (15) (2010) 154104, https://doi.org/10.1063/1.3382344.

[48] R. Nada, J.B. Nicholas, M.I. McCarthy, A.C. Hess, Basis sets for Ab initio periodic hartree-fock studies of zeolite/adsorbate interactions: He, Ne, and Ar in silica sodalite, Int. J. Quantum Chem. 60 (1996) 809–820.

[49] M. Catti, G. Valerio, R. D. and M. C. Quantum-mechanical calculations of the solid-state equilibrium MgO + Alpha-Al2O3 MgAl2O4 (Spinel) versus pressure, Phys. Rev. B 49 (1994) 14179–14187.

[50] A. Schäfer, C. Huber, R. Ahlrichs, Fully optimized contracted gaussian basis sets of triple zeta valence quality for atoms Li to Kr, J. Chem. Phys. 100 (8) (1994) 5829–5835, https://doi.org/10.1063/1.467146.

[51] Dovesi, R.; Saunders, V.R.; Roetti, C.; Orlando, R. et al. CRYSTAL17 User's Manual. 2017.

[52] D.W. Breck, Zeolite Molecular Sieves: Structure. Chemistry, and Use, Wiley, New York, 1974.

[53] C. Paolucci, I. Khurana, A.A. Parekh, S. Li, A.J. Shih, H. Li, J.R. Di Iorio, J. D. Albarracin-Caballero, A. Yezerets, J.T. Miller, W.N. Delgass, F.H. Ribeiro, W. F. Schneider, R. Gounder, Dynamic multinuclear sites formed by mobilized copper ions in NOx selective catalytic reduction, 898 LP – 903, Sci. (80-.) 357 (6354) (2017), https://doi.org/10.1126/science.aan5630.

[54] M. Signorile, E. Borfecchia, S. Bordiga, G. Berlier, Influence of ion mobility on the redox and catalytic properties of Cu ions in zeolites, Chem. Sci. 13 (35) (2022) 10238–10250, https://doi.org/10.1039/D2SC03565K.

[55] G. Turnes Palomino, A. Zecchina, E. Giamello, P. Fisicaro, G. Berlier, C. Lamberti, S. Bordiga, Polycarbonylic and Polynitrosylic Species in CuI-Exchanged ZSM-5, β, Mordenite and Y Zeolites: Comparison with Homogeneous Complexes. In *12th International Congress on Catalysis*, in: A. Corma, F.V. Melo, S. Mendioroz, J.L. G. Fierro (Eds.), Studies in Surface Science and Catalysis, Vol. 130, Elsevier, 2000, pp. 2915–2920, https://doi.org/10.1016/S0167-2991(00)80914-3.

[56] K. Góra-Marek, A.E. Palomares, A. Glanowska, K. Sadowska, J. Datka, Copper sites in zeolites - quantitative IR studies, Microporous Mesoporous Mater. 162 (2012) 175–180, https://doi.org/10.1016/j.micromeso.2012.06.029.

[57] K.A. Tarach, M. Jablonska, K. Pyra, M. Liebau, B. Reiprich, R. Glaser, K. Gora-Marek, Effect of zeolite topology on NH3-SCR activity and stability of Cu-exchanged zeolites, Appl. Catal. B-Environ. (2021) 284, https://doi.org/10.1016/j.apcatb.2020.119752.